Symmetry Breaking of Tail-Clamped Filaments in Stokes Flow

Jian Deng
State Key Laboratory of Fluid Power and Mechatronic Systems, Department of Mechanics, Zhejiang University, Hangzhou 310027, People's Republic of China

Xuerui Mao*
Faculty of Engineering, the University of Nottingham, University Park, Nottingham NG7 2RD, United Kingdom

Luca Brandt
Swedish e-Science Research Centre and Linné FLOW Centre, Department of Engineering Mechanics, KTH, SE-100 44 Stockholm, Sweden

(Received 7 September 2020; revised 14 November 2020; accepted 19 February 2021; published 22 March 2021)

Symmetry breaking (SB) of fluid-structure interaction problems plays an important role in our understanding of animals' locomotive and sensing behaviors. In this Letter, we study the SB of flexible filaments clamped at one end and placed in a spanwise periodic array in Stokes flow. The equilibrium state of the filament along the streamwise direction loses stability and experiences two-dimensional and then three-dimensional SBs as the spanwise distance increases, or as the filament rigidity reduces. For slightly deformed filaments, the viscous and pressure forces are commensurate, while for extremely deformed filaments the viscous force becomes dominant.

DOI: 10.1103/PhysRevLett.126.124501

In nature, animals benefit from their flexible organs to, for example, increase the swimming or flying efficiency by using flexible fins [1–3] or wings [4,5], propel bacteria by using flagella [6–9], sense the ambient fluid flows by flexible whiskers [10,11] [see Figs. 1(a) and 1(b)]. Functionalities mimicking these biological systems are of tremendous interest to develop smart artificial devices, such as energy extractors [12,13] and highly sensitive sensors [14].

The swimming or flying mechanisms for fish or birds can be explained by the spontaneous symmetry breaking (SB) of a flow configuration when inertia takes the dominant role over viscous forces at higher Reynolds numbers [15–18]. For instance, a flexible filament with a pinned head is deflected, transits to periodically flapping, and eventually to a chaotic state [15,19], as we increase the Reynolds number or reduce the rigidity of the filament, due to the Kelvin-Helmholtz instability. An inverted filament (clamped at the tail) can also experience the same route of SB [20–22]. In all these cases, without exception, the Reynolds number is a critical parameter, which determines the flow regime, e.g., a periodic flow, favored by efficient swimming, flying, or energy harvesting.

However, at the microscopic scales, for example, swimming bacteria with flagella, the Reynolds numbers range from 10^{-4} to 10^{-2}, and the flows are governed by the incompressible Stokes equations [23]. Similarly, the Stokes approximation can be applied when designing highly sensitive flow sensors. For example, it was shown that a cricket's clavate hair is able to sense airflows with velocity amplitudes down to 30 μm/s, with hair lengths of 20–250 μm, implying extremely low Reynolds numbers [11,24,25]. The SB of Stokes flow around such sensors with large aspect ratios, which will be modeled as flexible filaments in the following, is universal. For example, the whiskers of a cat are symmetric [see Fig. 1(a)], yet tiny disturbance on one side of the body, e.g., the motion of a mouse, causes SB.

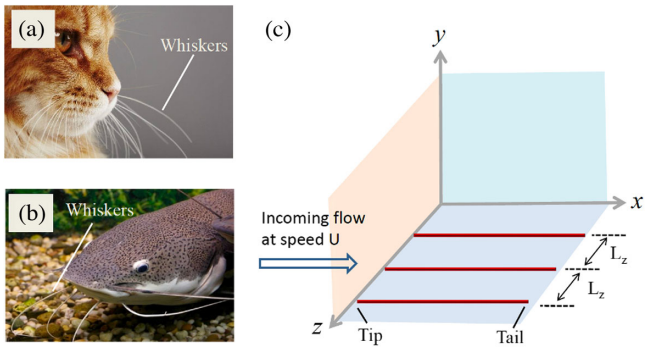

FIG. 1. The animals' whiskers, for example (a) cats and (b) catfish present an important class of tactile sensors that complement the functionalities of skin for detecting the ambient fluid flows with high sensitivity. (c) Schematic plot of the computational setup. The filament is clamped at the tail with $(x, y, z) = (1, 0, 0)$ and the tip is initially located at (0,0,0). The spanwise (z) extension of the domain is L_z and periodic boundary conditions are applied. Here the computational domain is repeated twice to illustrate the layout.

In the Stokes regime, the combined effect of hydrodynamic forces arising from the viscous medium coupled with the filament slenderness-induced flexibility (or softness) can result in geometrically nonlinear deformed configurations [26–29]. There have been extensive studies on the spontaneous oscillatory motion in the forms of either traveling or helical waves arising in clamped filaments owing to the buckling instability [6,9,29,30]. Unsurprisingly, the active contribution from the molecular motor forces was thought to be the key element to induce an instability [31]. Recently, by using a model with coupled elastohydrodynamics and motor kinetics [32], though confined in two dimension, Chakrabarti and Saintillan [33] reported that the motor activity drives a Hopf bifurcation leading to traveling wave solutions that propagate from tip to base. Moreover, they revealed the existence of a second transition far from equilibrium, where nonlinearities cause a reversal of the direction of the wave propagation and produce a variety of waveforms that resemble the beating patterns of swimming spermatozoa [33]. Nevertheless, we also know that without considering active forces, the balance between elastic and viscous forces only can promote buckling transitions of an elastic filament from a straight line to bending, even periodically oscillating states, in specific surrounding flows [30,34]. This passive response of a filament to its ambient flow, particularly in the Stokes regime, is fascinating due to the possibility that it can uncover the physical mechanisms behind the synchronous behaviors of swimming microorganisms, and their unique capability of sensing the environment, which, however, have not been well understood.

In this Letter, we report the bifurcation induced SB of clamped flexible filaments in Stokes flow. As the filament rigidity reduces or the spanwise distance between filaments increases, these lose stability of the original equilibrium position and bend in other stable equilibrium positions first constrained in a two-dimensional (2D) plane and then fully three-dimensional (3D). While the pressure is critical to the bending of filaments at finite Reynolds number [35], in Stokes flows, the pressure and viscous effects are commensurate in balancing the elastic force when the bending is at small scales.

The Cartesian system is adopted with x, y, and z denoting the streamwise, normal and spanwise directions, respectively. Initially the filament is placed along the x direction and its tail is clamped. Assuming the filament has the same density as the fluid, this initial position represents an equilibrium state. In the spanwise direction, periodic boundary conditions are applied and the domain size is denoted as L_z (normalized by the filament length), within which a single filament is contained, as schematically plotted in Fig. 1(c), where the domain is duplicated in the spanwise direction to clarify the computational setup. A uniform velocity $\boldsymbol{U}_\infty$ is prescribed at the inlet and far-field boundaries of the computational domain. The pressure is fixed at the outlet boundary.

The fluid flow is governed by the nondimensional Stokes equation:

$$\nabla^2 \boldsymbol{u} - \boldsymbol{\nabla} p + \boldsymbol{f} = 0 \quad \text{with} \quad \boldsymbol{\nabla} \cdot \boldsymbol{u} = 0, \tag{1}$$

where $\boldsymbol{u}$ is the velocity normalized by the free-stream velocity $\boldsymbol{U}_\infty$, p is pressure normalized by $\mu \boldsymbol{U}_\infty / L$, with μ and L denoting the dynamic viscosity and the length of the filament, and $\boldsymbol{f}$ is the forcing imposed by the filament to the fluid. The inertial term is not shown as we always integrate Eq. (1) until the solution becomes steady.

An immersed boundary method is used to model the flexible filament, whose governing equations can be written as [35,36]

$$\frac{\partial^2 \mathbf{X}}{\partial t^2} = \frac{\partial}{\partial s}\left(T \frac{\partial \mathbf{X}}{\partial s}\right) - \frac{\partial^2}{\partial s^2}\left(\gamma \frac{\partial^2 \mathbf{X}}{\partial s^2}\right) - \boldsymbol{F}, \tag{2}$$

where γ is the rigidity of the filament and s is the coordinate along the filament, with $s = 0$ and $s = 1$ representing the tip and the tail, respectively. T is the axial tension obtained by applying the inextensibility constraint to the filament $\partial \mathbf{X}/\partial s \cdot \partial \mathbf{X}/\partial s = 1$. $\boldsymbol{F}$ is the forcing imposed by the fluid on the filament and can be computed as

$$\boldsymbol{F} = \alpha \int_0^t (\boldsymbol{U}_{ib} - \boldsymbol{U}) dt' + \beta (\boldsymbol{U}_{ib} - \boldsymbol{U}), \tag{3}$$

where $\boldsymbol{U}_{ib}$ is the interpolated fluid velocity on the filament, $\boldsymbol{U}$ is the velocity of the filament, and α and β are negative constants. $\boldsymbol{F}$ can be spread to the fluid mesh using the four-point Dirac delta function to obtain $\boldsymbol{f}$ [37]. We note that the forcing term represented by Eq. (3) is a feedback to the

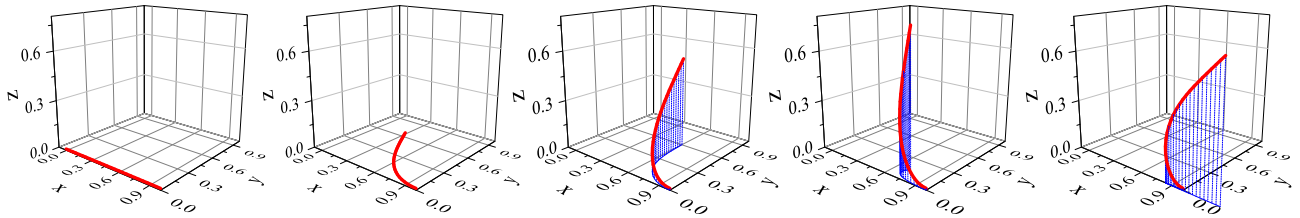

FIG. 2. Filament bending with $\gamma = 0.1$ for various L_z. The blue dotted lines show the projection onto the x–y plane.

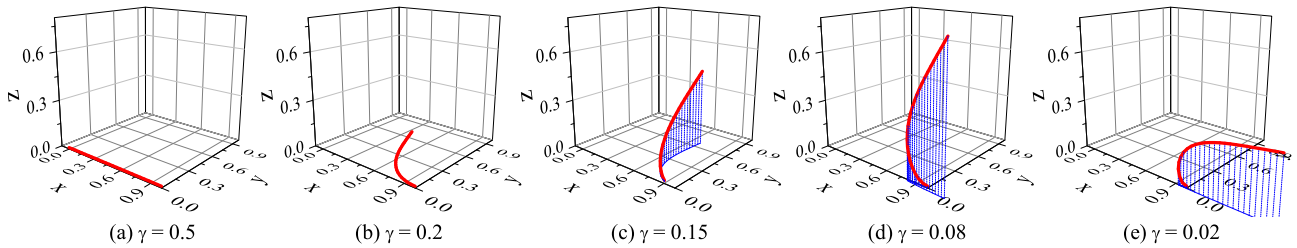

FIG. 3. Filament bending with $L_z = 0.64$ and various γ. The blue dotted lines show the projection onto the x–y plane.

difference $\boldsymbol{U}_{ib} - \boldsymbol{U}$ that asymptotically enforces $\boldsymbol{U}_{ib} = \boldsymbol{U}$ on the immersed boundary.

Validations of the numerical results against theoretical [38,39] and experimental [40] ones can be found in the Supplemental Material [41]. In addition, the results are validated against the solution of another solver adopting a different algorithm [42] and the difference is within 1%. Clearly this numerical setup is parameterised by the rigidity γ and the filament's spanwise distance L_z. At each combination of these parameters, the governing Eqs. (1) and (2) are evolved until reaching a steady solution before collecting data as presented below. Here, $L_z \in [0.08, 2.56]$: at $L_z = 0.08$, the overall fluid and filament dynamics is essentially 2D, and the spanwise periodically placed filaments can be regarded as 2D flags, whereas, for $L_z > 2.56$, the interactions between filaments become negligible and the results can be assumed not to change for higher L_z.

As shown in Fig. 2(a), at $\gamma = 0.1$, when $L_z = 0.08$, the filament is stable at the initial equilibrium position along x. At larger L_z, the filament loses stability and bends in the x–y plane to reach another equilibrium position, which will be denoted as 2D-SB in the following [see Fig. 2(b)]. For even larger L_z, the filament loses symmetry in the z direction and deviates from the x–y plane, which will be denoted as 3D-SB [see Figs. 2(c), 2(d), 2(e)]. As shown in Fig. 3, 2D-SB and 3D-SB are also observed at fixed L_z when reducing γ. From Fig. 1(a), whiskers of cats without SB and with 2D-SB can be clearly identified, while in the whiskers of catfish shown in Fig. 1(b), both 2D-SB and 3D-SB can be seen. To illustrate the flow field, we present in Fig. 4 the three-dimensional streamlines around the filament for the case in Fig. 2(c). The attached flow around the filament can be clearly seen.

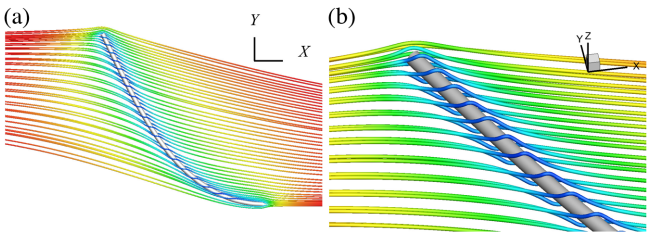

FIG. 4. (a) 3D streamlines around the filament with $\gamma = 0.1$ and $L_z = 0.32$; (b) enlarged view around the tip. The streamlines are colored by the magnitudes of the velocities, with blue and red representing the minimum and maximum.

The position of the tip of the filament are shown in Fig. 5 in the $\gamma - L_z$ plane. The x coordinate describes the scale of the deformation, whereas $y > 0$ and $z > 0$ illustrate the onset of 2D-SB and 3D-SB. Because of the symmetry of the numerical setup, negative y and z are not considered. At $\gamma = 0.5$, the filament is rigid enough and no bending is observed even at the largest L_z, while at $\gamma = 0.05$, 2D SB appears even at the smallest L_z. The threshold lines for 2D-SB and 3D-SB can be approximated as straight lines on the $\lg(\gamma) - \lg(L_z)$ plane at low values of L_z and converge to $\gamma = 0.4$ and $\gamma = 0.25$ at $L_z > 2$. Clearly the 2D-SB threshold line breaks the space into a symmetric part and an asymmetric one, which is further partitioned by the 3D-SB threshold line to 2D-SB and 3D-SB regions.

The 2D SB can be related to the buckling instabilities, following the classical theories [43,44]. The critical shear buckling load can be estimated as $Q_{\mathrm{cr}} = 7.837\gamma/L^2$, while the critical concentrated tip load $Q_{\mathrm{cr}} = 2.47\gamma/L^2$ [45]. The details of the derivation can be found in the Supplemental Material [41]. Here, we choose six typical cases, and redistribute the viscous force evenly along the filament, or impose it as a concentrated load onto the tip. As shown in Fig. 5(b), the onset of 2D SB predicted by the buckling instability analysis agrees very well with our numerical simulations.

As reported previously, the morphological transition and transport of an elastic filament can be characterized by an elastoviscous number η, which measures the flow strength relative to viscously modulated elastic relaxation of the filament [46–48]. Accordingly, we define here $\eta = 8\pi\tau L^3/\gamma$, where τ is the averaged viscous shear force on the filament. Interestingly, we find that η is almost constant (in the range of 199–201) on the 2D SB line shown in Fig. 5(b).

The force acting on the filament is of interest for the reduced order modeling of filament dynamics and the simulations of flow around a large number of filaments. This force consists of a tangental term from the viscous shear stress and a normal term from the pressure difference integrated over the cross section, denoted as F_μ and F_p, respectively. While the latter is dominant at finite Reynolds number [35,42], the former is expected to be critical in the

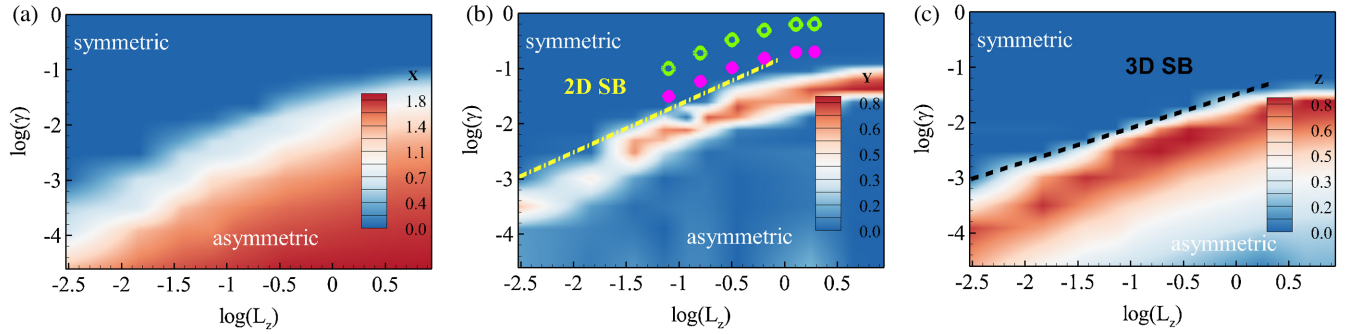

FIG. 5. (a),(b), and (c) Contours of the x, y, z position of the filament's tip on the $\log(\gamma) - \log(L_z)$ plane. $y > 0$ and $z > 0$ represent 2D-SB and 3D-SB, respectively. The threshold of 2D-SB and 3D-SB can be approximated as $\log(\gamma) = 0.97\log(L_z) + 0.58$ and $\log(\gamma) = 0.68\log(L_z) - 1.5$, denoted as the dash-dotted straight line in (b) and the dashed straight line in (c), at low L_z and approach $\gamma = 0.4$ and $\gamma = 0.25$, at $L_z > 2$. The purple dots in (b) represent the critical points calculated by buckling instability analyses based on distributed viscous forces, while the green circles are based on concentrated tip loads.

current Stokes flow. To verify this, we display the distribution of viscous and pressure forces from the tip ($s = 0$) to the tail ($s = 1$) in Figs. 6(a) and 6(b). Three typical cases illustrated in Fig. 3, with $L_z = 0.64$ and $\gamma = 0.2$, 0.08, and 0.02, are considered. The first case shows a small-scale deformation with the tip upstream of the filament. At $\gamma = 0.08$ and $\gamma = 0.02$, the tip is downstream of the tail, at $x = 1.17$ and $x = 1.7$, respectively, and the most upstream position, where the filament bends over, is at $s = 0.7$ and 0.9.

Clearly, the viscous forces only dominate for $\gamma = 0.02$, while in the other two cases, the viscous and pressure forces are commensurate. It has been proposed that if the filaments are dense and with small-scale deformations, such as in a hairy coated surface, the force around the tip is much larger than that on the body of the filaments [49,50]. The present study reveals that the pressure reaches maximum at the most upstream position, which is the tip when the deformation is small ($s = 1$ at $\gamma = 0.2$) and moves towards the tail at larger-scale deformations ($s = 0.7$ and 0.9 at $\gamma = 0.2$, 0.08); the viscous force varies mildly from the tip to the tail.

The moments generated by the viscous and pressure forces with respect to the tail are also plotted [see Figs. 6(c) and 6(d)]. The moments attain their maximum at $s = 0$, with the viscous component taking over as γ decreases. These data indicate that the tip force is critical to study the deformation of the filament related with the moments, but

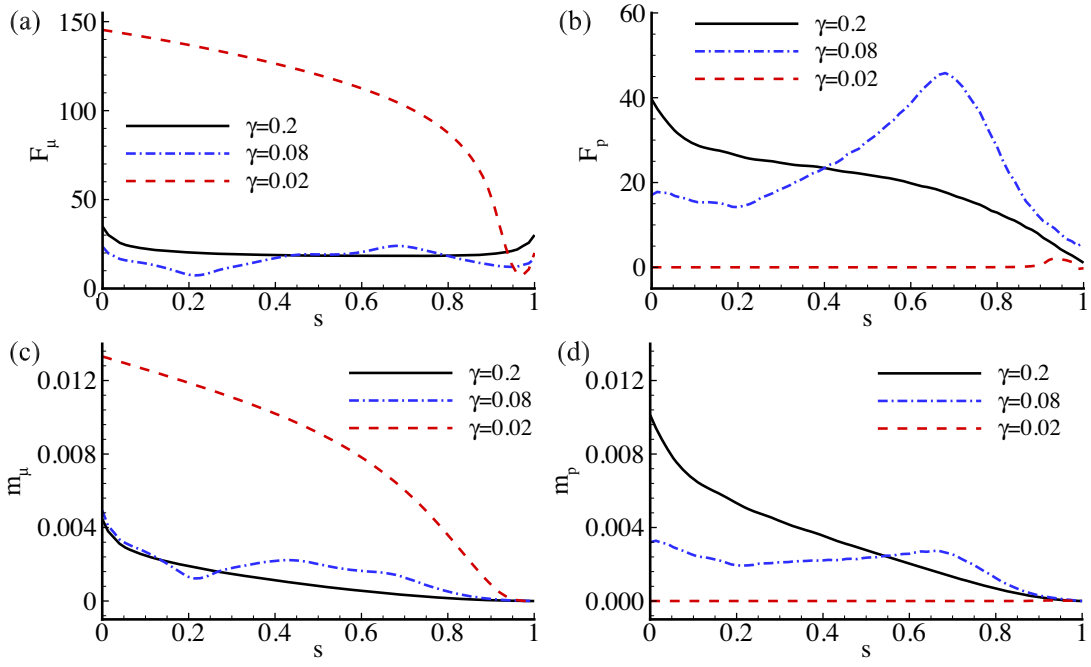

FIG. 6. Distribution of viscous force (F_μ) and pressure force (F_p), and their moments (m_μ and m_p) with respect to the tail at $L_z = 0.64$.

inadequate for the fluid and structure interactions associated with the forces.

In summary, the symmetry breaking of flexible filaments in Stokes flow is numerically studied. The filaments, with rigidity γ, are clamped on one end and placed periodically with spanwise distance L_z. When increasing L_z, the flow becomes increasingly 3D, the spanwise interaction of filaments reduces and the filaments are prone to lose stability of the original equilibrium position: 2D SB and 3D SB are observed in sequence when increasing the spacing and when reducing γ following a similar path. These forms of SBs are ubiquitous in nature and can be clearly identified from e.g., the whiskers of animals. The threshold for the 2D and 3D SB can be approximated as straight lines in the $\log\gamma - \log L_z$ plane at low L_z, whereas they approach $\gamma = 0.4$ and 0.25 at $L_z > 2$ when filament-filament interactions become negligible, in good agreement with buckling stability theory. As the deformation becomes larger, the viscous force takes over the pressure force to dominate the fluid and structure interactions, and the maximum of the force moves from the tip to the most upstream position of the filament.

Future extension of the present work may be devoted to instabilities and interactions between filaments in a non-Newtonian fluid matrix, in which case the relaxation time of the fluid microstructures will add nontrivial effects to those already discussed here.

This work was supported by the Marie Sklodowska-Curie Research and Innovation Staff Exchanges programme (Grant No. 777717). J. D. has been supported by the National Natural Science Foundation of China (Grants No. 11772299, No. 11922212).

*Corresponding author.
xuerui.mao@nottingham.ac.uk

[1] J. Zhang, N.-S. Liu, and X.-Y. Lu, J. Fluid Mech. **659**, 43 (2010).
[2] G.-J. Li and X.-Y. Lu, J. Fluid Mech. **712**, 598 (2012).
[3] S. Wang, G. He, and X. Zhang, Acta Mech. Sin. **32**, 980 (2016).
[4] S. Ramananarivo, R. Godoy-Diana, and B. Thiria, Proc. Natl. Acad. Sci. U.S.A. **108**, 5964 (2011).
[5] G. A. Tzezana and K. S. Breuer, J. Fluid Mech. **862**, 871 (2019).
[6] K. Sekimoto, N. Mori, K. Tawada, and Y. Y. Toyoshima, Phys. Rev. Lett. **75**, 172 (1995).
[7] G. Jayaraman, S. Ramachandran, S. Ghose, A. Laskar, M. S. Bhamla, P. B. Sunil Kumar, and R. Adhikari, Phys. Rev. Lett. **109**, 158302 (2012).
[8] E. Lauga, Annu. Rev. Fluid Mech. **48**, 105 (2016).
[9] D. Sarkar and S. Thakur, J. Chem. Phys. **146**, 154901 (2017).
[10] K. Takei, Z. Yu, M. Zheng, H. Ota, T. Takahashi, and A. Javey, Proc. Natl. Acad. Sci. U.S.A. **111**, 1703 (2014).
[11] H. Droogendijk, M. J. de Boer, R. G. Sanders, and G. J. Krijnen, J. R. Soc. Interface **11**, 20140438 (2014).
[12] S. Michelin and O. Doaré, J. Fluid Mech. **714**, 489 (2013).
[13] K. Shoele and R. Mittal, J. Fluid Mech. **790**, 582 (2016).
[14] M. Asadnia, A. G. P. Kottapalli, K. D. Karavitaki, M. E. Warkiani, J. Miao, D. P. Corey, and M. Triantafyllou, Sci. Rep. **6**, 32955 (2016).
[15] J. Zhang, S. Childress, A. Libchaber, and M. Shelley, Nature (London) **408**, 835 (2000).
[16] S. Bagheri, A. Mazzino, and A. Bottaro, Phys. Rev. Lett. **109**, 154502 (2012).
[17] J. Deng and C.-c. P. Caulfield, J. Fluid Mech. **787**, 16 (2016).
[18] J. Deng and C.-c. P. Caulfield, J. Fluid Mech. **840**, 688 (2018).
[19] L.-B. Jia and X.-Z. Yin, Phys. Fluids **21**, 101704 (2009).
[20] D. Kim, J. Cossé, C. H. Cerdeira, and M. Gharib, J. Fluid Mech. **736**, R1 (2013).
[21] J. Ryu, S. G. Park, B. Kim, and H. J. Sung, J. Fluids Struct. **57**, 159 (2015).
[22] H. Huang, H. Wei, and X.-Y. Lu, J. Fluid Mech. **837**, 461 (2018).
[23] E. Lauga and T. R. Powers, Rep. Prog. Phys. **72**, 096601 (2009).
[24] J. A. Humphrey, R. Devarakonda, I. Iglesias, and F. G. Barth, Phil. Trans. R. Soc. B **340**, 423 (1993).
[25] T. Shimozawa, T. Kumagai, and Y. Baba, J. Comp. Physiol. A **183**, 171 (1998).
[26] L. Turner, W. S. Ryu, and H. C. Berg, J. Bacteriol. **182**, 2793 (2000).
[27] M. T. Brown, B. C. Steel, C. Silvestrin, D. A. Wilkinson, N. J. Delalez, C. N. Lumb, B. Obara, J. P. Armitage, and R. M. Berry, J. Bacteriol. **194**, 3495 (2012).
[28] K. Son, J. S. Guasto, and R. Stocker, Nat. Phys. **9**, 494 (2013).
[29] M. K. Jawed and P. M. Reis, Soft Matter **12**, 1898 (2016).
[30] L. Guglielmini, A. Kushwaha, E. S. Shaqfeh, and H. A. Stone, Phys. Fluids **24**, 123601 (2012).
[31] D. J. Smith, E. Gaffney, H. Gadêlha, N. Kapur, and J. Kirkman-Brown, Cell Motil. Cytoskeleton **66**, 220 (2009).
[32] D. Oriola, H. Gadêlha, and J. Casademunt, R. Soc. Open Sci. **4**, 160698 (2017).
[33] B. Chakrabarti and D. Saintillan, Phys. Rev. Fluids **4**, 043102 (2019).
[34] R. E. Goldstein, E. Lauga, A. I. Pesci, and M. R. E. Proctor, Phys. Rev. Fluids **1**, 073201 (2016).
[35] W.-X. Huang, S.-j. Shin, and H. Jin-Sung, J. Comput. Phys. **226**, 2206 (2007).
[36] M. E. Rosti, A. A. Banaei, L. Brandt, and A. Mazzino, Phys. Rev. Lett. **121**, 044501 (2018).
[37] C. Peskin, Acta Numer. **11**, 479 (2002).
[38] J. Burgers, Kon. Ned. Akad. Wet. Verhand **16**, 1 (1938).
[39] G. Batchelor, J. Fluid Mech. **44**, 419 (1970).
[40] T. Ui, R. Hussey, and R. Roger, Phys. Fluids **27**, 787 (1984).
[41] See Supplemental Material at http://link.aps.org/supplemental/10.1103/PhysRevLett.126.124501 for the validations for the numerical code by examining the Stokes drag force on a straight filament, and the detailed derivation of the critical load for buckling instability.

[42] J. Deng, X. Mao, and F. Xie, Phys. Rev. E **100**, 053107 (2019).
[43] B. Chakrabarti, Y. Liu, J. LaGrone, R. Cortez, L. Fauci, O. du Roure, D. Saintillan, and A. Lindner, Nat. Phys. **16**, 689 (2020).
[44] D. B. Stein, G. De Canio, E. Lauga, M. J. Shelley, and R. E. Goldstein, Phys. Rev. Lett. **126**, 028103 (2021).
[45] M. Bakker, J. Eng. Mech. **132**, 1160 (2006).
[46] Y.-N. Young and M. J. Shelley, Phys. Rev. Lett. **99**, 058303 (2007).
[47] N. Quennouz, M. Shelley, O. Du Roure, and A. Lindner, J. Fluid Mech. **769**, 387 (2015).
[48] Y. Liu, B. Chakrabarti, D. Saintillan, A. Lindner, and O. Du Roure, Proc. Natl. Acad. Sci. U.S.A. **115**, 9438 (2018).
[49] J. Alvarado, J. Comtet, E. Langre, and A. Hosoi, Nat. Phys. **13**, 1014 (2017).
[50] J. Sundin and S. Bagheri, J. Fluid Mech. **861**, 556 (2019).